AGU100 ADVANCING EARTH AND SPACE SCIENCE

JGR Planets

RESEARCH ARTICLE
10.1029/2019JE006092

Special Section:
Studies of the 2018/Mars Year 34 Planet-Encircling Dust Storm

Key Points:
- We show how the ionospheric peak altitude at Mars varies during six different dust storms
- The peak altitude rises 10–15 km during each dust storm
- Dust storms increase the peak altitude's variability, suggesting they enhance dynamical processes coupling the lower and upper atmospheres

Correspondence to:
Z. Girazian,
zachary-girazian@uiowa.edu

Citation:
Girazian, Z., Luppen, Z., Morgan, D. D., Chu, F., Montabone, L., Thiemann, E. M. B., et al. (2019). Variations in the ionospheric peak altitude at Mars in response to dust storms: 13 years of observations from the Mars Express Radar Sounder. *Journal of Geophysical Research: Planets*, *124*, e2019JE006092. https://doi.org/10.1029/2019JE006092

Received 17 JUN 2019
Accepted 17 SEP 2019
Accepted article online 19 SEP 2019

Variations in the Ionospheric Peak Altitude at Mars in Response to Dust Storms: 13 Years of Observations From the Mars Express Radar Sounder

Z. Girazian[1], Z. Luppen[1], D. D. Morgan[1], F. Chu[1], L. Montabone[2], E. M. B. Thiemann[3], D. A. Gurnett[1], J. Halekas[1], A. J. Kopf[1], and F. Němec[4]

[1]Department of Physics and Astronomy, University of Iowa, Iowa City, IA, USA, [2]Space Science Institute, Boulder, CO, USA, [3]Laboratory for Atmospheric and Space Physics, University of Colorado Boulder, Boulder, CO, USA, [4]Faculty of Mathematics and Physics, Charles University, Prague, Czech Republic

Abstract Previous observations have shown that, during Martian dust storms, the peak of the ionosphere rises in altitude. Observational studies of this type, however, have been extremely limited. Using 13 years of ionospheric peak altitude data from the Mars Advanced Radar for Subsurface and Ionosphere Sounding instrument on Mars Express, we study how the peak altitude responded to dust storms during six different Mars years (MY). The peak altitude increased ~10–15 km during all six events, which include a local dust storm (MY 33), three regional dust storms (MYs 27, 29, and 32), and two global dust storms (MYs 28 and 34). The peak altitude's orbit-to-orbit variability was exceptionally large at the apexes of the MY 29 and MY 32 dust seasons and dramatically increased during the MY 28 and MY 34 global dust storms. We conclude that dust storms significantly increase upper atmospheric variability, which suggests that they enhance dynamical processes that couple the lower and upper atmospheres, such as upward propagating gravity waves or atmospheric tides.

Plain Language Summary Limited observations have shown that dust storms at Mars significantly affect the upper atmosphere and ionosphere. In particular, the expansion of the atmosphere in response to solar heating of dust causes fixed pressure levels in the upper atmosphere to rise in altitude. The peak of the ionosphere–where the maximum electron density occurs–can be used as a diagnostic of this expansion because it forms at a fixed pressure level in the upper atmosphere (120–150 km). In this work, we use 13 years of observations from the radar sounder on the Mars Express spacecraft to evaluate how the peak altitude of the ionosphere varied during six different dust storms. We found that the peak altitude increased by 10–15 km during each dust storm. Additionally, the orbit-to-orbit variability of the peak altitude increased significantly during the dust storms, which suggests that dynamical processes that couple the lower and upper atmospheres were enhanced.

1. Introduction

Dust storms have proven to be an important source of atmospheric variability at Mars. Dust particles lifted into the atmosphere are heated by solar radiation, which causes the atmosphere to expand and global circulation patterns to change (Bougher et al., 1997; Haberle et al., 1993; Heavens et al., 2011; Wolkenberg et al., 2018). Dust also affects the distribution of water vapor, which has consequences for atmospheric photochemistry, hydrogen escape, and climate evolution (Chaffin et al., 2017; Daerden et al., 2019; Heavens et al., 2018; Krasnopolsky, 2019; Vandaele et al., 2019). Although the dust itself is mostly confined to altitudes below 80 km (Clancy et al., 2010), the effects of the dust extend well into the thermosphere (>100 km)—even to geographic locations that are far from where the dust originated (Liu et al., 2018; Withers & Pratt, 2013).

The response of the thermosphere to lower atmospheric dust is generally marked by a rapid increase in the neutral density at a fixed altitude, followed by a slow density decay back to nominal levels over several weeks (England & Lillis, 2012; Keating et al., 1998; Lillis et al., 2010; Withers & Pratt, 2013; Zurek et al., 2017). During typical dust events, thermospheric neutral densities increase by a factor of ~1.5–3.0 at fixed altitudes (Liu et al., 2018; Withers & Pratt, 2013; Zou et al., 2016), but thermospheric neutral temperatures do not drastically change at fixed pressure levels (Fang et al., 2019; McElroy et al., 1977; Wang & Nielsen, 2003).

When thermospheric pressure surfaces rise in response to dust loading, the peak of the ionosphere—which typically forms between 120 and 150 km and at a fixed pressure level (Withers, 2009)—rises in altitude.

Elevated ionospheric peak altitudes during dust storms have been observed by radio occultation (RO) experiments on several spacecraft, the first being Mariner 9, which arrived at Mars in 1971 during a global event. Mariner 9 observed that, during the global dust storm, the ionospheric peak altitude was ~20 km higher than usual (Hantsch & Bauer, 1990) and then slowly decayed back to typical values during the dust storm's waning stages (Withers & Pratt, 2013). The RO experiments on the Mars Global Surveyor (MGS) and Mars Atmosphere and Volatile EvolutioN (MAVEN) spacecraft have also observed the ionospheric peak rise during regional dust storms. MGS observed the peak rise ~5 km during a dust storm at solar longitude (L_s) 130° in Mars Year (MY) 27 (Qin et al., 2019; Withers & Pratt, 2013), and MAVEN observed the peak rise ~10 km during a dust storm at $L_s \sim 305°$ in MY 33 (Withers et al., 2018).

Motivated by the limited amount of observations showing how the ionospheric peak responds to dust storms, we utilize a 13-year span of peak altitude measurements from the Mars Advanced Radar for Subsurface and Ionosphere Sounding (MARSIS) instrument on Mars Express (MEX; Gurnett et al., 2005; Picardi et al., 2004). By combining these data with dust optical depth measurements from the same time period (Montabone et al., 2015), we investigate how dust affected the ionospheric peak altitude during six different MYs. In two of these years, MY 28 and MY 34, there was a global dust storm. Our objectives are (1) to compare the response of the peak altitude during six different dust storms and (2) to determine if dust storms affect the variability of the peak altitude.

The paper is organized as follows. In section 2, we present the theory that describes the formation of the ionospheric peak and explain how variations in the ionospheric peak altitude can be used to estimate changes in the thermospheric pressure. In section 3, we describe the data sets that are used in our analysis. In section 4, we show how dust affected the peak altitude during several MYs. In section 5, we discuss our results and present our conclusions.

2. Theory of the Ionospheric Peak Altitude

The main peak of the Martian ionosphere is well described by Chapman theory (Chapman, 1931; Girazian & Withers, 2013; Mendillo et al., 2017; Schunk & Nagy, 2009; Withers, 2009). Chapman theory predicts that, under photochemical equilibrium conditions, the ionospheric peak forms at the altitude where the optical depth of ionizing extreme ultraviolet (EUV) photons is equal to 1 (Breus et al., 2004; Withers, 2009). Mathematically, this is approximated by

$$n(h_{\max})\sigma H \sec\chi = 1, \tag{1}$$

where $n(h_{\max})$ is the neutral CO_2 density at the peak altitude $h_{\max}$, σ is the CO_2 absorption cross section at EUV wavelengths, H is the neutral scale height, and χ is the solar zenith angle (SZA). Equation (1) requires many simplifying assumptions to be valid (Schunk & Nagy, 2009; Withers, 2009) but has proven to be an adequate description of the ionospheric peak at Mars (Fallows et al., 2015; Girazian & Withers, 2013; Mendillo et al., 2017; Withers, 2009). Using equation (1), several studies have shown that observed changes in the ionospheric peak altitude can be used to estimate variations in the thermospheric neutral density or pressure (Bougher et al., 2001; 2004; Qin et al., 2019; Withers & Pratt, 2013; Zou et al., 2011; 2016).

For our purposes, we are interested in using equation (1) to quantify how the peak altitude rises or falls in response to changes in the thermospheric pressure. Equation (1) is derived under the assumption of a static, isothermal atmosphere so that it can be recast as

$$n_0 e^{-(h_{\max}-h_0)/H}\sigma H \sec\chi = 1, \tag{2}$$

where n_0 is the neutral density at some reference altitude h_0. If n_0 or H changes, $h_{\max}$ must rise or fall such that equation (2) remains satisfied:

$$n_{0_1} e^{-(h_{\max_i}-h_0)/H_i} H_i = n_{0_f} e^{-(h_{\max_f}-h_0)/H_f} H_f, \tag{3}$$

where the subscripts i and f represent the initial and final states, respectively. In equation (3), we have removed the SZA dependence by assuming that it is fixed. Next, by setting the reference altitude to h_0 =

10.1029/2019JE006092

$h_{\max_i}$, equation (3) becomes

$$\frac{n_{0_f} H_f}{n_{0_i} H_i} = \exp\left(\frac{\Delta h_{\max}}{H_f}\right), \tag{4}$$

where $\Delta h_{\max} = h_{\max_f} - h_{\max_i}$. According to equation (4), if we assume that $H_i = H_f$, then a factor of ~3 increase in n_0 results in the peak altitude increasing by one scale height. Furthermore, equation (4) states that increases in the neutral density or scale height during dust storm onset will cause the peak altitude to rise, while decreases in the density or scale height during the waning stages of a dust storm will cause the peak altitude to fall.

Equation (4) can also be recast in terms of atmospheric pressure. The pressure is given by $P = \rho g H$, where P is pressure, ρ is mass density, and g is the gravitational acceleration, which is assumed to be constant. This equation for atmospheric pressure is equivalent to the ideal gas law for an isothermal atmosphere with a fixed scale height H. The assumption of a fixed H is used throughout this work because observations and modeling suggest that dust storms significantly affect thermospheric densities but only modestly affect thermospheric temperatures (Fang et al., 2019; Liu et al., 2018; Qin et al., 2019; McElroy et al., 1977; Wang & Nielsen, 2003). This assumption does, however, add uncertainty to our analysis.

Substituting the pressure into equation (4) gives

$$\frac{P_f}{P_i} = \exp\left(\frac{\Delta h_{\max}}{H}\right). \tag{5}$$

Here, P_i and P_f are the atmospheric pressures at the ionospheric peak and H has been assumed to not change. Equation (5) states that, at a fixed SZA, the peak altitude forms at a constant atmospheric pressure level. Equation (5) was used in the study by Withers and Pratt (2013) to estimate changes in the thermospheric pressure during the waning stages of the Mariner 9 dust storm.

In addition to allowing one to quantify how the peak altitude responds to changes in the thermospheric density, scale height, or pressure, equations (1), (4), and (5) summarize the conditions that control variations in the ionospheric peak altitude. Equation (1) can be inverted to show that the peak altitude increases with increasing SZA proportional to ln(sec χ), indicating a steep rise in the peak altitude near the day-night terminator (Fallows et al., 2015; Withers, 2009). Equation (5) describes how the peak altitude can vary with latitude and local time due to diurnal pressure gradients in the thermosphere (Bougher et al., 2015; Zou et al., 2011) and further shows that any physical process that alters the thermospheric pressure will also alter the peak altitude. These processes include but are not limited to (1) the annual variation in solar irradiance at Mars due to its large orbital eccentricity; (2) atmospheric tides and waves; (3) solar EUV heating; and (4) atmospheric circulation patterns. All of these processes must be considered when attempting to identify variations in the peak altitude caused solely by dust storms.

3. Data

We use three types of data: ionospheric peak altitudes from the MARSIS radar sounder, dust optical depths compiled from several instruments, and solar EUV irradiances from an empirical model. In this section, we describe each data set and our processing techniques.

3.1. Peak Altitudes

Ionospheric peak altitudes are derived from MARSIS radar sounding observations. MARSIS sounds the ionosphere during the periapsis segment of the ~7-hr, near-polar orbit of MEX. When MARSIS sounds the ionosphere, it transmits radio pulses and records the return echoes from pulses that are reflected off the ionosphere. The transmitter sweeps through 160 quasi-logarithmically spaced frequencies between 0.1 and 5.4 MHz over 1.257 s. Each sweep produces an ionogram—the echo intensity as a function of frequency and time delay. MARSIS makes frequency sweeps every 7.54 s, while MEX is below ~1,500 km, returning several hundred ionograms during each periapsis pass.

Figure 1a shows an ionogram from 16 May 2018. The vertical stripes at low frequencies are a common feature; they are produced by electron plasma oscillations induced by the radio transmitter during ionospheric soundings. The spacings between the stripes are used to determine the local electron density at the spacecraft location (Duru et al., 2008; Gurnett et al., 2005; 2008). The thin horizontal stripe between ~1.0 and

10.1029/2019JE006092

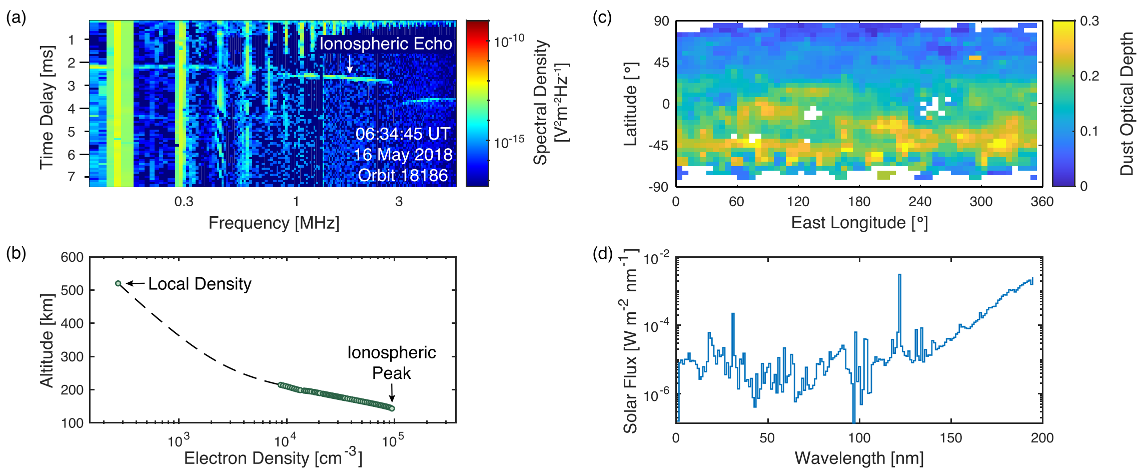

Figure 1. Examples of the four data products used in our study, all of which are from 16 May 2018. (a) MARSIS ionogram showing the vertical stripes at low frequencies used to derive the local electron density, and the ionospheric echo that captures the electron density down to the ionospheric peak. (b) The electron density profile derived from the MARSIS ionogram shown in Panel a. The dashed line marks the measurement gap as explained in the text. (c) The dust optical depth map from Montabone et al. (2015). (d) The solar extreme ultraviolet spectrum from the Flare Irradiance Spectral Model-Mars (Thiemann et al., 2017). MARSIS = Mars Advanced Radar for Subsurface and Ionosphere Sounding.

3.0 MHz is the ionospheric echo, which represents radar pulses that were reflected off the ionosphere below ~200 km (Gurnett et al., 2005; 2008). The highest frequency of the ionospheric echo, near 3 MHz in this example, is the reflection from the ionospheric peak. The time delay at this frequency in the ionospheric trace is related to the altitude of the peak. The horizontal stripe at frequencies greater than 3 MHz, with a time delay of ~4 ms, is the return echo from the surface of Mars.

If an ionogram provides a local electron density measurement, and also has a clear ionospheric trace, then it can be inverted into an altitude profile of the electron density. The inversion procedure requires one to make an assumption about the shape of the electron density profile between the altitude of MEX, where the local density is measured, and the altitude of the first electron density measurement in the ionospheric trace. In this work, we adopt the inversion technique described in Němec et al. (2016), which assumes that the shape of the density profile within the measurement gap is characterized by a lower and upper topside scale height, with a smooth transition between them. Figure 1b shows the electron density profile that was derived by applying this technique to the ionogram shown in Figure 1a. Once inverted into an electron density profile, the peak altitude is easily extracted as marked in Figure 1b.

We use MARSIS ionograms obtained between 11 July 2005 and 14 July 2018. All of the ionograms obtained up to 22 May 2016 were inverted into electron density profiles. Only a subset of the ionograms obtained after 22 May 2016 were used, because they have not yet been inverted into electron density profiles due to the time-consuming and hands-on processing techniques that are required (Gurnett et al., 2008; Morgan et al., 2008). In lieu of this, we have inverted two subsets of ionograms from after this date specifically for this study. The first subset of ionograms is from the month of January 2017. This month was targeted because elevated peak altitudes were observed by the MAVEN RO experiment during a dust storm (Withers et al., 2018). The second subset is from 14 May 2018 to 14 July 2018. This period was targeted because it covers a significant portion of the 2018 global dust storm (Guzewich et al., 2019; Vandaele et al., 2019).

After inverting the ionograms into electron density profiles and extracting their peak altitudes, we filter the data set based on several criteria. First, we keep density profiles only if they monotonically decrease with increasing altitude, which is a requirement of the Němec et al. (2016) inversion technique. Second, we remove any peak altitudes below 80 km or above 220 km, well outside the expected peak altitude and likely the result of bad inversions (Fox & Weber, 2012; Němec et al., 2016; Vogt et al., 2017; Withers, 2009). Third, we limit the profiles to times when MEX was below 1,000 km. After applying these criteria, the complete data set includes more than 180,000 peak altitude measurements from 2,401 MEX orbits.

Uncertainties in the peak altitudes are, at best, ±7 km, as determined by the intrinsic 91.4-μs time resolution of the MARSIS receiver. The Němec et al. (2016) inversion technique also adds to this uncertainty, given that it relies on an assumption about the shape of the electron density profile within the measurement gap.

In section 4, we analyze orbit-averaged peak altitudes (from a limited SZA range) and assign uncertainties based strictly on the spread of the observed peak altitudes during each orbit. In particular, for each orbit, we define the uncertainty in the orbit-averaged peak altitude as the standard deviation of the peak altitudes used to calculate the average.

3.2. Dust Optical Depths

Dust optical depth maps are derived by combining measurements from several instruments, as described in Montabone et al. (2015). The maps provide a continuous measure of the dust content in the lower atmosphere, with good coverage in latitude, longitude, and L_s from 1999 until present. The dust data for the time period considered here are synthesized from infrared observations by the Mars Odyssey Thermal Emission Imaging System (Christensen et al., 2004) and the Mars Reconnaissance Orbiter Mars Climate Sounder (MCS; McCleese et al., 2007). The maps provide the optical depth at 9.3-μm absorption, normalized to an atmospheric pressure level of 610 Pa. An example of a dust optical depth map is shown in Figure 1c.

Throughout this work, we use the observation-only dust maps that sometimes have incomplete coverage in latitude and longitude (Montabone et al., 2015). We also use dust maps that were developed specifically for the MY 34 global dust storm and this special issue. These MY 34 dust maps use estimated column dust opacities from MCS as described in detail in Montabone et al. (2019). We use the v2.5 version of the maps.

We assign a “local” average and global average dust optical depth to each MARSIS electron density profile. The local average accounts for our expectation that the ionospheric peak will respond to dust storms that are nearby. The global average accounts for our expectation that the ionospheric peak might also respond to dust storms that are far away, due to their effects on atmospheric circulation (Bell et al., 2007; Withers & Pratt, 2013; Withers et al., 2018). To assign the global average, we match each MARSIS electron density profile with the dust optical depth map from the closest date and then average the dust optical depth map over all latitudes and longitudes. Since the dust maps have a resolution of $\sim 1°$ in L_s, the global average dust optical depth is constant during each MEX orbit. We assign the local average in a similar way but only after restricting the dust data to the latitude range of the MARSIS observations during each orbit.

3.3. Solar EUV Irradiances

Solar EUV irradiances are from the Flare Irradiance Spectral Model-Mars, which is an empirical model that provides daily averaged solar EUV spectra at Mars (Thiemann et al., 2017). The spectra have 1-nm resolution and cover wavelengths between 0.5 and 189.5 nm. An example Flare Irradiance Spectral Model-Mars spectrum, from 16 May 2018, is shown in Figure 1d.

We assign a single number measure of the EUV irradiance (W/m^2) to each MARSIS electron density profile. We do this by first matching each electron density profile with the solar EUV spectrum from the closest date, then integrating the matched EUV spectrum over wavelengths between 0.5 and 92.5 nm. The cutoff wavelength of 92 nm is chosen because it is the longest wavelength photon that can ionize O and CO_2, which are the most abundant neutral species in the thermosphere of Mars (Girazian & Withers, 2013; 2015; Mahaffy et al., 2015; Schunk & Nagy, 2009).

3.4. Overview of the Data

Figures 2a–2c show the 13-year time series of ionospheric peak altitudes along with the SZAs and geographic latitudes of the MARSIS observations. Data gaps are present throughout the time series because MARSIS frequently toggles between ionospheric and subsurface sounding modes and does not make observations during eclipse seasons when there is insufficient sunlight to recharge the MEX solar panels. The error bars in Panels b and c show the $\sim 80°$ in latitude and the $\sim 30°$ in SZA that MARSIS covers during a typical periapsis pass. We also note that, from one periapsis pass to the next, the observational SZA and latitude are nearly identical, but the longitude is shifted by $\sim 100°$.

Figure 2d shows the solar EUV irradiance and the inverse-square of the Mars-Sun distance during the MARSIS observations. The latter is representative of the solar insolation at Mars, which varies annually due to the planet's eccentric orbit around the Sun. The 13-year period covers more than a complete solar cycle, starting with the declining phase of Solar Cycle 23 in 2005, and continuing through the declining phase of Solar Cycle 24 in 2018. The EUV irradiance varies over the 11-year solar cycle, reaching a minimum in 2008, a maximum in 2014, and also annually due to the varying Mars-Sun distance.

Figure 2e shows the global average dust optical depth from the same time period. The repeated peaks in the optical depth during each Martian year are the signature of the well-known annual dust cycle at Mars

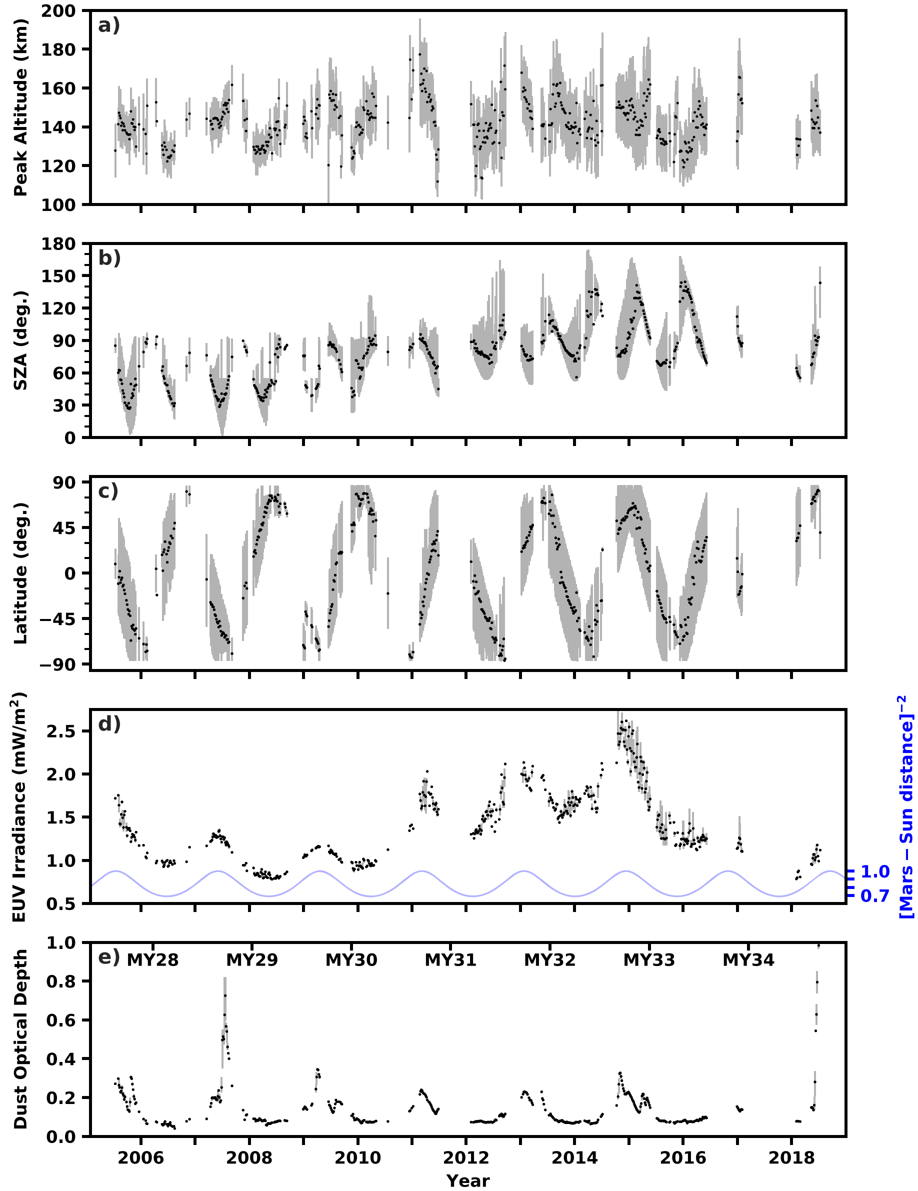

Figure 2. Time series of the data used in this study. The (a) ionospheric peak altitudes from MARSIS, (b) their solar zenith angles (SZA), and (c) their geographic latitudes. (d) The solar EUV irradiance and the inverse square of the Mars-Sun distance (normalized). (e) The globally averaged dust optical depths (τ) during the MARSIS observations. The black circles in each panel are averages from 16 Mars Express orbits (120 hr). The error bars in Panels a, d, and e show the standard deviations from within each averaging bin, while the error bars in Panels b and c show the complete spread in the data within each averaging bin. MARSIS = Mars Advanced Radar for Subsurface and Ionosphere Sounding; SZA = solar zenith angle; EUV = extreme ultraviolet.

(Fang et al., 2019; Montabone et al., 2015). During most years, the optical depth reaches a maximum between L_s 210° and 240°, and then exhibits a smaller, secondary peak between L_s 300° and 340°. Exceptions to the typical annual dust cycle are seen in MYs 28 and 34, when global dust storms caused large spikes in the dust optical depth at atypical L_s values (Guzewich et al., 2019; Montabone et al., 2015; 2019; Sánchez-Lavega et al., 2019; Wolkenberg et al., 2018).

Now that we have provided an overview of the data used in our study, we are ready to focus on our science objectives, which are (1) to compare the response of the peak altitude during six different dust storms and (2) to determine if dust storms affect the variability of the peak altitude. In the next section, we will focus on these objectives by closely examining how the ionospheric peak altitude responded to dust storms during

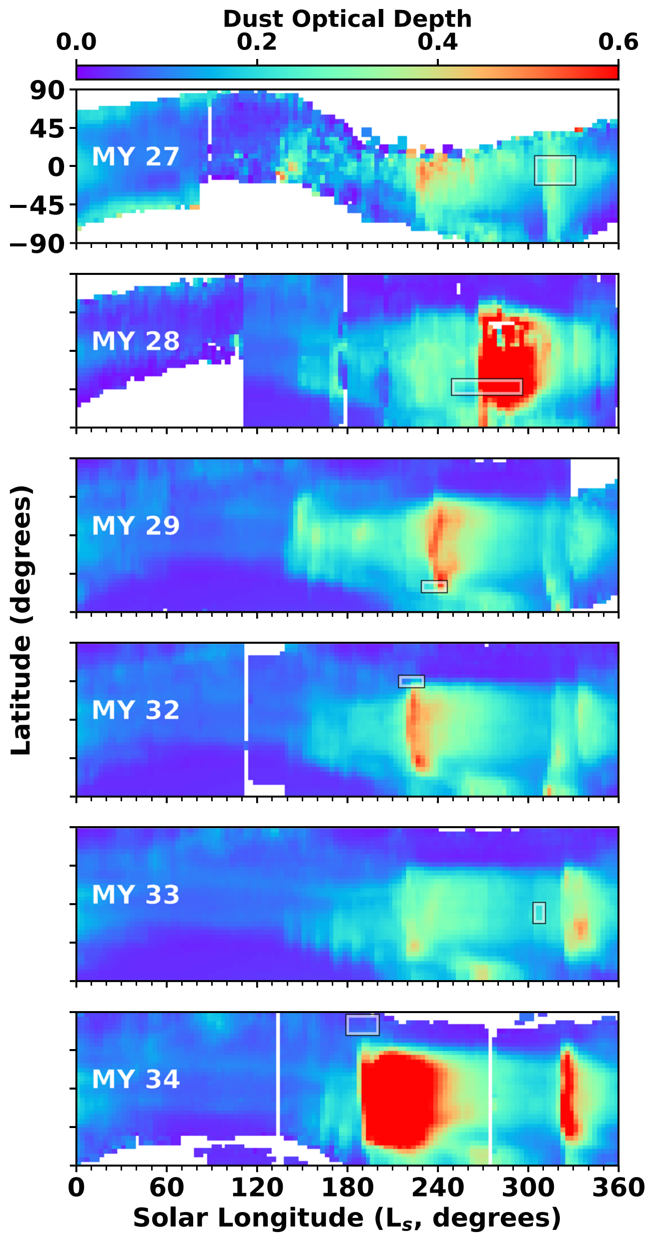

Figure 3. Complete dust maps from the six Mars years during which we analyze MARSIS peak altitudes. The rectangles in each panel mark the L_s and latitude coverage of the MARSIS observations. MARSIS = Mars Advanced Radar for Subsurface and Ionosphere Sounding.

six different MYs. For each MY, we analyze a subset of MARSIS peak altitudes from a limited range of L_s and SZA. With the exception of MY 33, the L_s range is chosen to capture the onset of a dust storm, and the SZA range is chosen to capture the smallest SZAs observed by MARSIS during that period.

To provide global context, Figure 3 shows the complete dust maps from the six Martian years used in our anlaysis. Each panel in Figure 3 is marked with a rectangle that shows the L_s and latitude coverage of the MARSIS peak altitudes that we analyze during that Martian year. Figure 3 also highlights that, with the exception of MY 27, the dust maps have full latitudinal coverage during the time periods considered.

The observations in MYs 27–29 provide the most favorable conditions because MARSIS observations cover dayside SZAs < 55° during times when the global dust content significantly increases. The MY 29 observations at southern latitudes and the MY 32 observations at northern latitudes are from similar dust conditions.

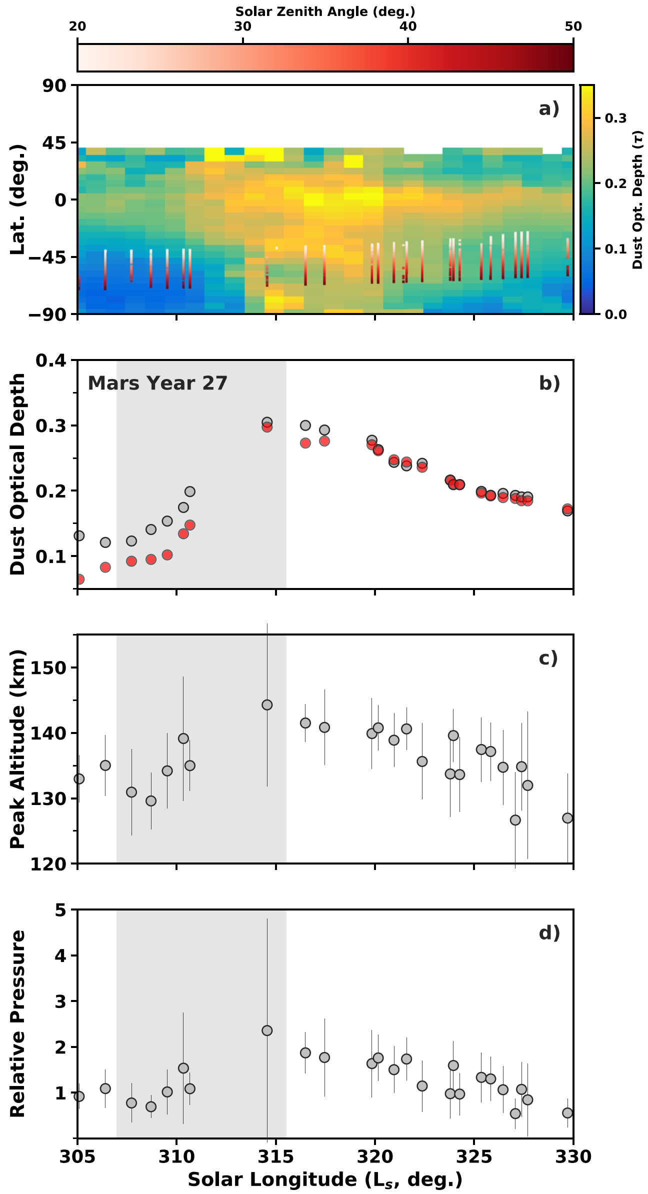

Figure 4. The MY 27 dust season at L_s 305° to 330°. (a) Dust optical depths averaged over 1° in L_s, 360° in longitude, and 5° in latitude. The MARSIS measurement coverage is plotted on top of the dust map, colored according to the solar zenith angle of the observation. Each vertical line represents the MARSIS latitudinal coverage from a single orbit. (b) Global average (gray) and local average (red) dust optical depths from orbits during which there were at least 10 MARSIS peak altitude measurements. (c) Orbit-averaged ionospheric peak altitudes. (d) Orbit-averaged relative pressures derived using equation (5) with a reference altitude of $h_{\max_i}$ = 134 km. The gray shaded regions mark the period when the peak altitude and relative pressure increases during the dust storm. MARSIS = Mars Advanced Radar for Subsurface and Ionosphere Sounding.

This allows us to compare the effects of dust in two different hemispheres. The MY 30 and MY 31 observations are not presented because dayside observations were not obtained during the onset of dusty periods. The MY 33 observations are specifically targeted to compare with MAVEN observations from the same period (Withers et al., 2018). Finally, the MY 34 observations, which are from northern polar latitudes, cover the onset of the MY 34 global dust storm.

Based on previous studies, we expect that high local dust content will elevate the peak altitude and that high global dust content may elevate the peak altitude due to its effects on atmospheric circulation patterns (Bell et al., 2007; Liu et al., 2018; Fang et al., 2019; Hantsch & Bauer, 1990; Qin et al., 2019; Withers & Pratt,

Table 1
Summary of the Observed Ionospheric Response to Dust for the Six Mars Years (MY) Analyzed in Section 4

MY	L_s	Year	Date	SZA	LAT	EUV	$\Delta\tau$	τ_{max}	Δh_{max}	$\sigma^i_{h_{max}}$	$\sigma^f_{h_{max}}$
27	305–330	2005	10/12 to 11/24	20–50	(−20, −70)	1.3	0.2	0.3	10–15	4	4
28	250–295	2007	06/03 to 08/14	30–40	(−50, −65)	1.6	0.6	1.2	10–15	4	10
29	230–245	2009	03/20 to 04/05	45–55	(−65, −75)	1.2	0.1	0.5	10–20	11	11
32	215–230	2014	10/16 to 11/10	75–80	(40, 50)	2.4	0.1	0.5	10-15	5	7
33	304–310	2017	01/23 to 02/21	70–80	(−20, −40)	1.1	0.0	0.2	~10	—	—
34	180–195	2018	05/22 to 06/26	60–85	(60, 85)	1.0	0.5	1.5	10-15	—	—

Note. Columns 2–6 list the solar longitudes (L_s, degrees), Earth years, dates (mm/dd), solar zenith angles (SZA, degrees), and minimum and maximum latitudes (LAT, degrees) of the Mars Advanced Radar for Subsurface and Ionosphere Sounding observations that were analyzed in each MY. Column 7 lists the EUV irradiance level (EUV, mW/m^2). Columns 8 and 9 summarize each dust storm, including the increase in the globally averaged dust optical depth ($\Delta\tau$) and the maximum equatorial-averaged (between ±30°) dust optical depth (τ_{max}). Columns 10–12 summarize the observed changes in the ionospheric peak, including its increase in altitude (Δh_{max}, km) and its variability before ($\sigma^i_{h_{max}}$, km) and after ($\sigma^f_{h_{max}}$, km) dust storm onset as defined throughout section 4.

2013; Zou et al., 2016). Additionally, increases in the peak altitude might be less noticeable during low solar EUV levels when the upper atmosphere is intrinsically more variable due to increased gravity wave activity (England et al., 2017; Terada et al., 2017; Harada et al., 2018; Siddle et al., 2019).

4. Peak Altitude Variations During Six Dust Storms

4.1. Mars Year 27

Figure 4 summarizes the observations from late in the MY 27 dust season between L_s 305° and 330°. In Figure 4a, the MARSIS observational coverage in latitude and SZA is plotted on top of the dust optical depth map. The MARSIS data from this time period are restricted to SZAs between 20° and 50° to rule out SZA being a significant factor in any observed peak altitude variations. The dust map shows a rapid increase in the atmospheric dust content starting at L_s 310° at most latitudes. Dust optical depth measurements at latitudes greater than +45° were unavailable during this period (Montabone et al., 2015). Figure 4b shows the global and local average dust optical depths (section 3.2) for each MEX orbit during which MARSIS obtained at least 10 peak altitude measurements. The optical depths increase sharply at $L_s \sim 305°$ and then slowly decline through $L_s \sim 320°$.

Figure 4c shows the corresponding orbit-averaged ionospheric peak altitudes, with error bars representing the spread in the peak altitude measurements (1σ) from each MEX orbit. The peak altitude rapidly rises 10–15 km between L_s 307° and 315° and then slowly descends back to pre–dust storm values over ∼ 15° of L_s. The peak altitude's rapid rise and slow descent is consistent with previous reports of the peak altitude's response to dust storms (Withers & Pratt, 2013; Withers et al., 2018).

Using the observed peak altitudes and equation (5), we can estimate how the thermospheric pressure changed during the dust storm (Withers & Pratt, 2013; Qin et al., 2019). In equation (5), we set $h_{\max_1}$ to a constant reference altitude equal to the average peak altitude prior to dust storm onset ($L_s < 307°$). Then, we set the neutral scale height, H, to a fixed value of 12 km, which is a typical value for the dayside thermosphere (Mahaffy et al., 2015; Withers, 2006; Zurek et al., 2017). This choice introduces some uncertainty in the derived pressure changes because H can vary between 8 and 16 km. With $h_{\max_1}$ and H fixed, equation (5) gives the pressure ratio, P_f/P_i, at every point where there is an orbit-averaged peak altitude. This method was used by Withers and Pratt (2013) to estimate thermospheric pressure changes during the Mariner 9 global dust storm. We adopt their terminology by calling P_f/P_i the "relative pressure" (P_{rel}).

The peak in the relative pressure, shown in Figure 4d, coincides with the maximum in the dust optical depth at $L_s \sim 315°$ and reaches a value of $P_{rel} = 2.4(\pm 2.4)$. The standard deviation of P_{rel} does not take into account the range of possible H values but is large due to the highly variable peak altitudes observed during this orbit. The maximum pressure increase of 2.4 is on the same order as the value derived during the waning stages of the Mariner 9 global dust storm (Withers & Pratt, 2013).

10.1029/2019JE006092

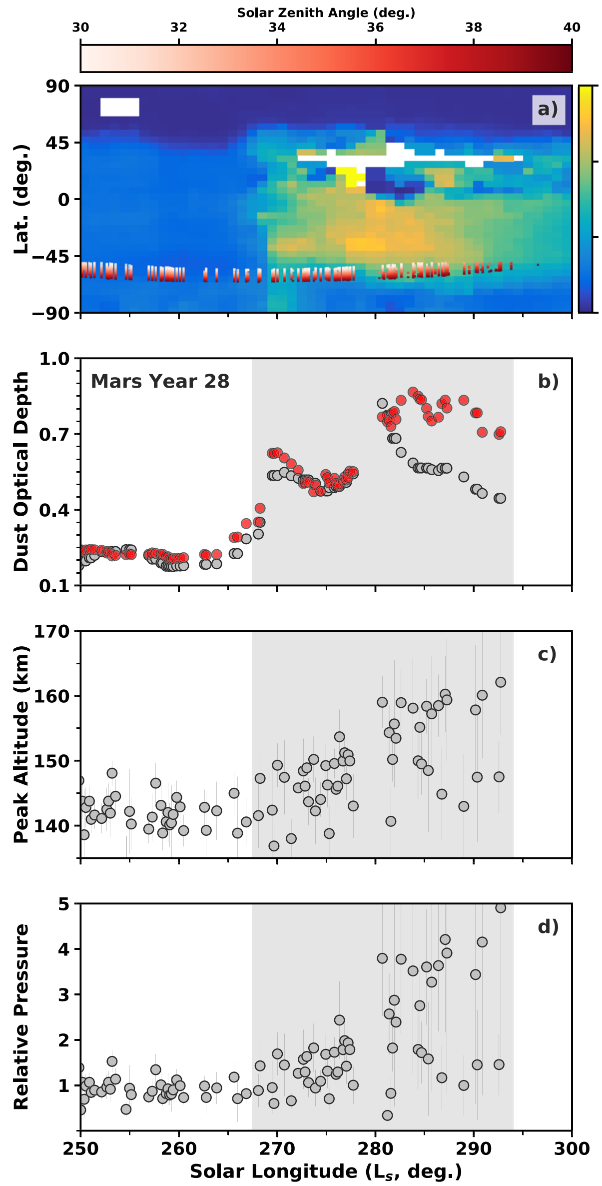

Figure 5. Similar to Figure 4 but showing observations from the MY 28 global dust storm and with the axes scaled differently. The relative pressure is derived using a reference altitude of $h_{\max_i} = 143$ km.

Next, we test if the variability of the peak altitude is affected by the dust storm. To accomplish this, we define a variability metric, $\sigma_{h_{\max}}$, and compare its value before and after dust storm onset. The metric is a measure of the peak altitude's orbit-to-orbit variability. We determine $\sigma_{h_{\max}}$ by first calculating the absolute differences between adjacent orbit-averaged peak altitudes, and then setting $\sigma_{h_{\max}}$ equal to the average of the differences within a specified L_s range. Using this procedure, we find that $\sigma_{h_{\max}} = 4$ km both before ($L_s < 312°$) and after ($L_s > 312°$) the peak of the storm. Thus, the dust storm did not significantly affect the variability of the peak altitude.

To conclude, the peak altitude increased by 10–15 km during the MY 27 dust storm, but the variability of the peak altitude was unaffected. This MY 27 case study is summarized in Table 1, which includes a description of the MARSIS observing conditions, the dust storm, and the response of peak altitude. Table 1 also includes a summary of the five other case studies presented throughout this section.

4.2. Mars Year 28

Figure 5 summarizes the observations from the MY 28 global dust storm between L_s 250° and 300°. During the global dust storm, the lower atmospheric dust content was atypically large and widespread around the planet (Montabone et al., 2015; Wolkenberg et al., 2018). As Figure 5a shows, the MARSIS data from this period are from SZAs 30–40°, and from southern latitudes between −50° and −65°. Figures 5a and 5b show that the local and global dust optical depths begin to increase at $L_s \sim 265°$ and reach maxima between $L_s \sim 275°$ and $\sim 280°$. The MARSIS observations do not cover the entire event because dust levels remained elevated through $L_s \sim 320°$ (Montabone et al., 2015; Wolkenberg et al., 2018).

The ionospheric peak altitude, shown in Figure 5c, begins to rise at the onset of the dust storm and continues to rise throughout the observational period. Furthermore, the variability of the peak altitude significantly increases after the peak of the dust storm ($L_s \sim 280°$). From before dust storm onset ($L_s < 265°$) to after the dust storm peak ($L_s > 280°$), $\sigma_{h_{\max}}$ more than doubles, increasing from 4 to 10 km. (Although not shown, we also note that the highly variable peak altitudes have no longitudinal trend).

Such variability was not observed in MY 27 (Figure 4), during which the MARSIS observations covered similar latitudes and SZAs but during which the dust optical depth was a factor of ~2 smaller (Figure 4). One possible explanation is that the atypically high dust levels during the MY 28 global dust storm increased upper atmospheric variability, perhaps by enhancing upward propagating waves, atmospheric circulation, or atmospheric tides (and references therein; Bell et al., 2007; Bougher et al., 2015; Medvedev et al., 2013). The relative pressure, shown in Figure 5d, is extremely variable after the peak of the dust storm, changing by as much as a factor of 15 across the time period, implying that the upper atmosphere is perturbed both spatially and temporally.

In summary, the peak altitude increased by 10–15 km and became highly variable during the MY 28 global dust storm.

4.3. Mars Year 29

Figure 6 summarizes a small number of observations from the peak of the MY 29 dust season between L_s 230° and 245°. As Figure 6a shows, the MARSIS observations during this period are from SZAs 45–55° and from southern latitudes between −65° and −75°. Figures 5a and 5b show that, at the start of the observing period, the dust optical depth is already higher than usual because the MY 29 dust season began several months earlier at L_s 170° (Figure 3). Nonetheless, the local and global dust optical depths increase by 0.1 between 235° and 245°.

The peak altitude, shown in Figure 6c, potentially increases between L_s 234° and 238°, but the trend is weak owing to the peak altitude's remarkable variability. The variability metric is $\sigma_{h_{\max}} = 11$ km throughout the entire period and does not change after the global average dust optical depth increases ($L_s > 238°$). The magnitude of the variability metric is comparable to that derived for the MY 28 global dust storm (section 4.2). The relative pressure, shown in Figure 6d, is also remarkably variable and changes by as much as a factor of 10.

Comparing the MY 29 and MY 27 (Figure 4) case studies reveals some stark differences. MY 27 is marked by low variability ($\sigma_{h_{\max}} = 4$ km), and the peak altitude exhibits a clear increase in tandem with the dust optical depth. Meanwhile, MY 29 is marked by such high variability ($\sigma_{h_{\max}} = 11$ km) that the increasing peak altitude trend is comparable to the orbit-to-orbit variations.

Differences in dust content during the MY 27 and MY 29 observational periods may explain these differences. The global dust optical depths in MY 27 rapidly increase by a factor of 3 (0.1–0.3) over 7° in L_s, while the optical depths in MY 29 increase by only a factor of 1.5 (0.25–0.35) over the same time period. Another consideration is that in MY 29 the dust season was well underway when the observing period began, which may explain the exceptional variability. To contrast this, the MY 27 dust storm was weaker overall (Figure 3), and the global dust content was smaller before the event began (it happened later in the year during the second peak of the annual dust cycle).

To conclude, the peak altitude may have increased by 10–20 km during the MY 29 dust storm, but the increase is comparable to the exceptionally high variability observed at that time.

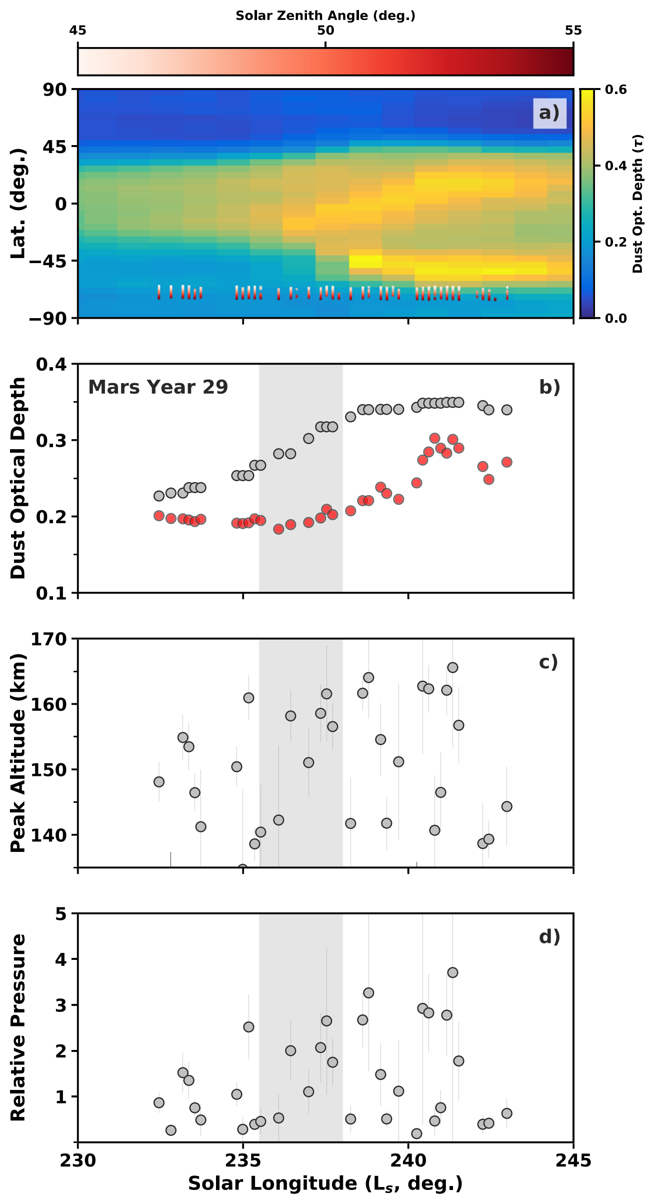

Figure 6. Similar to Figure 4 but showing observations from the MY 29 dust season and with the axes scaled differently. The relative pressure is derived using a reference altitude of $h_{\max_i} = 150$ km.

4.4. Mars Year 32

Figure 7 summarizes observations from the MY 32 dust season between L_s 215° and 230°. The observing conditions are very similar to those in MY 29 (Figure 6). In both cases, the dust level is already elevated when the observing period begins, and the dust optical depths increase by a factor of ~1.5 over ~ 10° of L_s. In MY 32, however, the MARSIS observations are now in the northern hemisphere instead of the southern hemisphere, and they cover a higher SZA range between 75° and 80°.

The peak altitude, shown in Figure 7c, increases 10–15 km between L_s 221° and 222° and is somewhat elevated through L_s 225°. However, similar to MY 29, it is difficult to conclusively determine if this trend is statistically significant because the peak altitude exhibits substantial variability. The variability metric is $\sigma_{h_{\max}} = 5$ km at $L_s < 221°$ and $\sigma_{h_{\max}} = 7$ km at $L_s > 223°$. The relative pressure, shown in Figure 7d, also exhibits substantial variability; it changes by as much as a factor of 8.

Although the variability is high in MY 32, it is not as high as in MY 29 ($\sigma_{h_{\max}} \simeq 7$ km vs. $\sigma_{h_{\max}} = 11$ km), which might be a consequence of the different latitudes of the observations. Both are from the southern spring

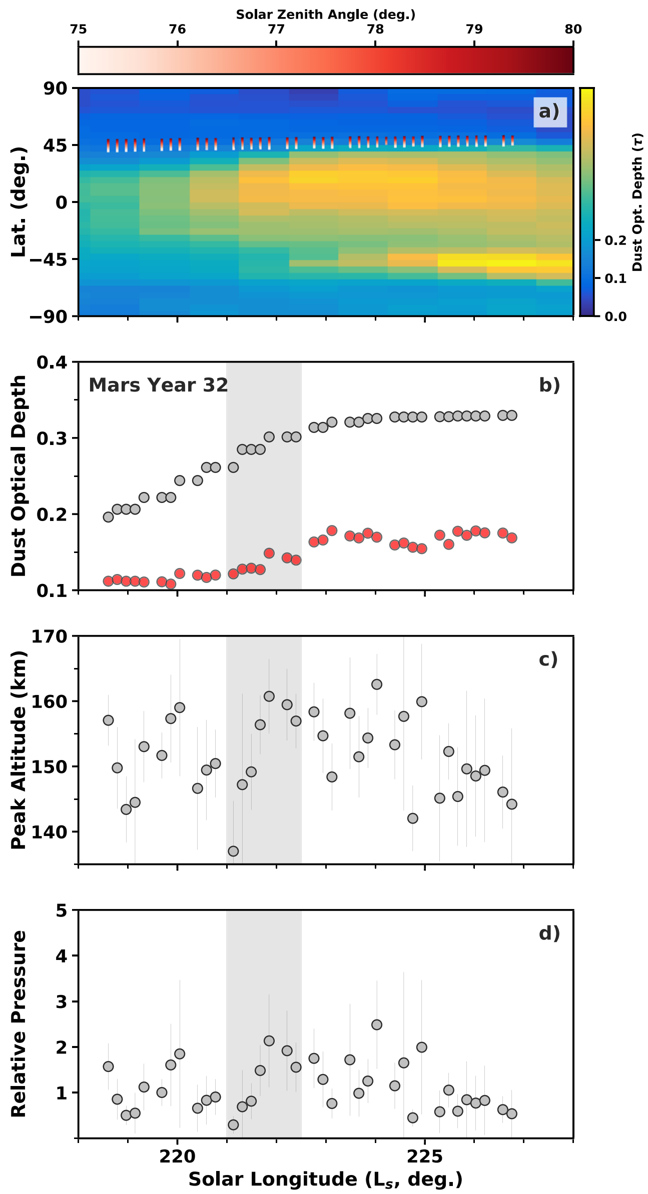

Figure 7. Similar to Figure 4 but showing observations from the MY 32 dust season and with the axes scaled differently. The relative pressure is derived using a reference altitude of $h_{\max_i}$ = 152 km.

season, but the MY 29 data are from the southern hemisphere, and the MY 32 data are from the northern hemisphere.

Another consideration is that the solar EUV irradiance was a factor of 2 smaller during the MY 29 than during the MY 32 period (2.4 vs. 1.2 mW/m^2, Figure 2d). The higher variability observed in MY 29, then, might be explained by increased atmospheric gravity wave activity. Gravity wave activity is anticorrelated with the thermospheric temperature (England et al., 2017; Harada et al., 2018; Terada et al., 2017). Given that the solar EUV heating rate was significantly smaller in MY 29, thermospheric temperatures were likely lower (Bougher et al., 2015; Thiemann et al., 2018), and strong gravity wave perturbations were likely present. These perturbations in the thermospheric pressure would drive significant variations in the ionospheric peak altitude (equation (5)), making the peak altitudes more variable in MY 29 than in MY 32.

If this hypothesis is correct, we might also expect higher variability in MY 27 when the EUV irradiance was only 1.3 mW/m^2. The peak altitude, however, is less variable in MY 27 ($\sigma_{h_{\max}}$ = 4 km) than in both MY 29 ($\sigma_{h_{\max}}$ = 11 km) and MY 32 ($\sigma_{h_{\max}} \simeq$ 7 km). This once again points to differences in the magnitudes of the

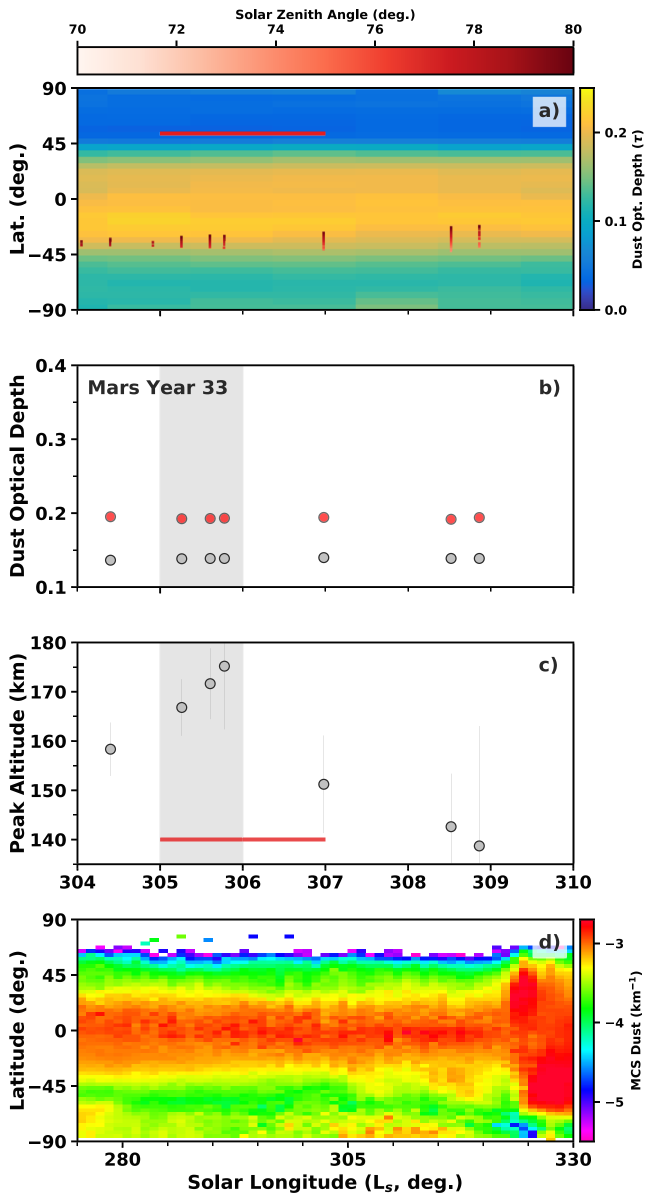

Figure 8. Similar to Figure 4 but showing observations from MY 33 during the time when the Mars Atmosphere and Volatile EvolutioN Radio Occultation Science Experiment (ROSE) observed the peak altitude rise during a localized dust storm (Withers et al., 2018). The horizontal red lines mark the latitudes of the ROSE observations (Panel a) and the L_s range when the peak was observed to rise (Panel c). Panel d shows a zoomed out map of the MCS dust extinction at 50 Pa (~25 km), which confirms the localized dust storm between $L_s \sim 305°$ and 315° and at latitudes $< -60°$ that was reported in Withers et al. (2018). MCS = Mars Climate Sounder.

dust storms. During the weak MY 27 dust storm, we observe a stable peak altitude that clearly increases in altitude, but during the relatively stronger MY 29 and MY 32 dust storms, we observe highly variable peak altitudes and less apparent peak altitude increases. This comparison suggests dust storms increase upper atmospheric variability and that the magnitude of the variability is proportional to the strength of the dust storm.

In summary, the peak altitude may have increased 10–15 km during the MY 32 dust storm, but, like MY 29, the increasing trend is comparable to the orbit-to-orbit variability.

4.5. Mars Year 33

Figure 8 shows a small subset of MARSIS observations from MY 33 between L_s 304° and 310°. Note that because there are so few observations, we are unable to analyze the peak altitude's variability during this period. The MARSIS observations, shown in Figure 8a, are from SZAs 70–80° and southern latitudes between −20° and −40°. These observations are specifically targeted in our study because Withers et al. (2018), using observations from the MAVEN Radio Occultation Science Experiment (ROSE), reported that the peak altitude increased ∼10 km between L_s 305° and 307° during a small, localized dust storm near the south pole. The ROSE observations were obtained at similar SZAs (∼ 75°), but at higher latitudes (53°N, Figure 8a).

Figures 8a and 8b show that, although the dust optical depths are slightly elevated compared to nondust season, they were constant throughout this period (Figures 2 and 3). Nonetheless, the peak altitude shown in Figure 8c increases from ∼160 to 175 km between L_s 304° and 306°, then falls sharply to 140 km by L_s 309°. The L_s in which the peak altitude rises coincides with the L_s range reported by Withers et al. (2018) for the MAVEN ROSE observations, as marked by the red line in Figure 8c.

Although our results are consistent with Withers et al. (2018), it is interesting that the dust optical depths used in our work do not show any dust increase during this time. Figure 4b in Withers et al. (2018) clearly shows that a small, localized dust storm near the south pole was observed by the MCS at L_s 305°. This inconsistency can likely be explained by considering two major differences in the dust data used. First, Withers et al. (2018) used MCS dust opacities at the specific pressure level of 50 Pa, while we use MCS estimated column dust optical depths, derived by integrating the MCS dust opacity over all available levels, including over the extrapolated part of the dust opacity profile down to the ground, assuming the dust is well mixed (Montabone et al., 2015). Second, recent analysis of MY 34 MCS column dust optical depths have highlighted large differences between dayside and nightside values during dust storms, with dayside values generally being larger (Montabone et al., 2019). While these differences are still a topic of ongoing research, the MY 33 reconstructed maps of column dust optical depth used in our work were constructed primarily from nightside MCS observations (Montabone et al., 2015). Hence, it is possible that the optical depths used in our work are low-biased such that the small, localized dust storm in MY 33 is missing from the maps.

For completeness, Figure 8d shows the MCS dust extinction map at L_s 275–330°. We produced the map by bin-averaging the MCS dust extinction data from the 50-Pa level (McCleese et al., 2007) over 3° in latitude and 1° in L_s. The map is nearly equivalent to Figure 4b in Withers et al. (2018) and confirms the small, localized dust storm near the south pole that started at L_s ∼ 305°.

It is also interesting to consider that the MAVEN ROSE observations are from northern latitudes near +50°, while the MARSIS observations are from southern latitudes near −30° (Figure 8a). Despite the large separation between them, both instruments observe the peak altitude rise at nearly the same time. This implies that the dust storm affected the upper atmosphere over large spatial distances on short timescales. Furthermore, compared to MARSIS, the MAVEN ROSE peak altitude descends more slowly after being elevated by the dust storm (see Figure 4 in Withers et al., 2018). This implies that the effects of the dust storm lasted longer in the northern hemisphere than in the southern hemisphere, despite the dust storm being localized near the south pole.

To summarize, the peak altitude increased ∼10 km during the MY 33 local dust storm.

4.6. Mars Year 34

Figure 9 summarizes the MARSIS observations from the MY 34 global dust storm between L_s 180° and 195°. The observations are somewhat unfavorable because the MEX periapsis segment covered high SZAs and was rapidly evolving toward the nightside. Consequently, the observational period covers from before the onset of the dust storm ($L_s \simeq$ 185°) to after it became a global event ($L_s \simeq$ 190°; Montabone et al., 2019). It does not cover the entirety of the storm as dust levels remained highly elevated through ∼ L_s 240° (Figure 3). Given the constraints of the observations, we slightly modify our analysis for this event.

The MARSIS observations, shown in Figure 8a, are from SZAs 60–85° and northern polar latitudes between +59° and +86°. The global average dust optical depth, shown in Figure 9b, begins to rapidly increase at L_s ∼185°, from ∼0.15 before dust storm onset, to 0.6 by L_s 197°. The local average dust optical depth, however, is relatively constant, indicating that the lower atmospheric dust content at northern polar latitudes, where the MARSIS observations are from, did not significantly increase. In Figure 8b we also show a third type of averaged optical depth, which we derive by averaging the dust data from a confined latitude range between +0° and 45°. This "northern hemisphere" average optical depth is a better indicator of dust at locations near the peak altitude observations. Figure 8b shows that the northern hemisphere dust optical depth increases

10.1029/2019JE006092

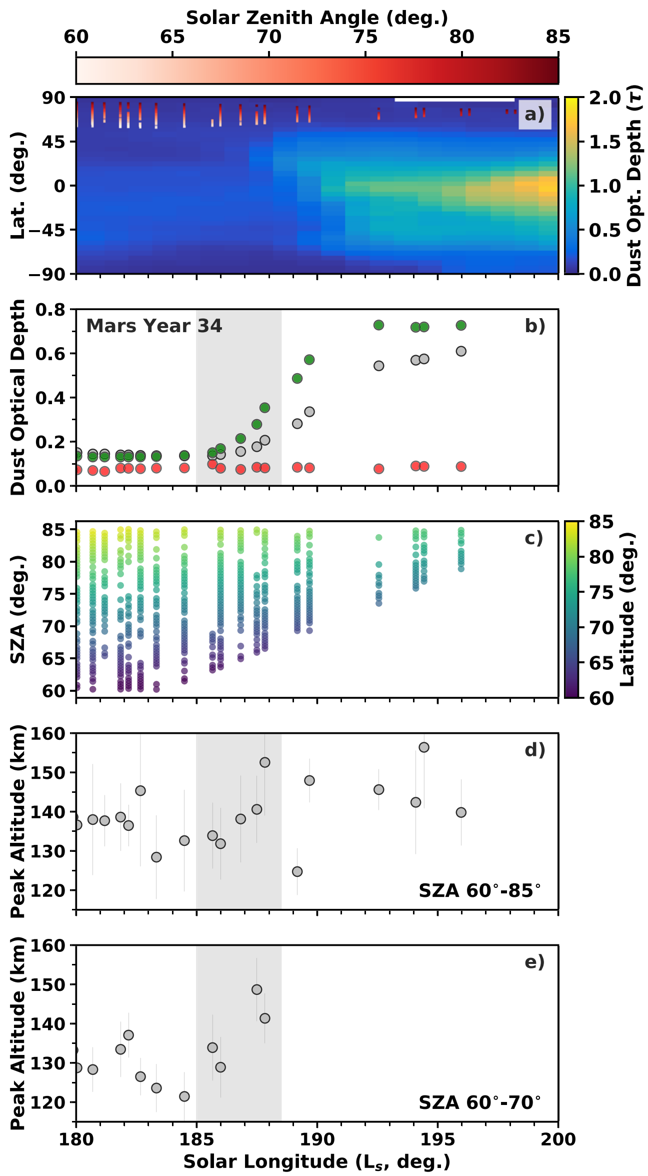

Figure 9. Observations from the MY 34 global dust storm. Panels a and b are the same as in Figure 4, but the northern hemisphere averaged dust optical depth (latitudes 0–45°) was added to Panel b (green circles). (c) The SZAs and latitudes of the Mars Advanced Radar for Subsurface and Ionosphere Sounding measurements. (d) Orbit-averaged peak altitudes for SZAs 60–85°. (e) Orbit-averaged peak altitudes for SZAs 60–70°. SZA = solar zenith angle.

more rapidly than the local or global dust optical depths, a consequence of the dust storm having originated in the northern hemisphere near +30° (Sánchez-Lavega et al., 2019).

Figure 9c highlights the limitations of the SZA and latitude coverage during this period. The beginning of the period contains measurements from the southernmost latitudes (< 65°) that are closest to where the dust storm originated. Also, after L_s 187°, the SZA range is skewed toward higher and higher values with each passing orbit. Since the peak altitude is strongly dependent on SZA near the terminator (equation (1)), we must be careful when analyzing the peak altitudes from this period. Therefore, we calculate orbit-averaged peak altitudes from two different SZA ranges: 60–85° and 60–70°.

The peak altitude at SZAs between 65° and 85°, shown in Figure 9d, rises 10–15 km between L*s* 185° and 188°. The increase occurs at the onset of the dust storm when the northern hemisphere dust optical depth increases from 0.15 to 0.35. Following its increase, the peak altitude becomes highly variable. Between L_s 188° and 190°, the peak altitude decreases from 153 (± 14) km to 125 (± 6) km, then increases to 148 (± 6) km the next orbit. Using equation (5) with $h_{\max_i} = 137$ km, these peak altitude changes correspond to relative pressures of 4.0 (± 4.0), 0.4 (± 0.2), and 3.0 (± 1.0), respectively. The variability metric also increases from $\sigma_{h_{\max}} = 5$ km ($L_s < 185°$) to $\sigma_{h_{\max}} = 11$ km ($L_s > 189°$), but this increase is not necessarily meaningful because the metric is being compared across two periods that have vastly different SZA coverage (Figure 9c).

The peak altitude at SZAs between 60° and 70° is shown in Figure 9e. In this case, we require five or more peak altitude observations to calculate an orbit-average (as opposed to 10 or more in Figure 9d). Again, the peak altitude rises 10–15 km between 185° and 188°, concurrent with the increase in the northern hemisphere dust optical depth. The two different SZA ranges (Figures 9c and 9d) provide ample evidence that the peak altitude increased at the onset of the MY 34 global dust storm between L_s 185° and 188°.

MAVEN ROSE also observed peak altitudes during the MY 34 global dust storm, but at a later time period between L_s 195° and 270° (Felici et al., 2019). The observed peak altitudes in both the northern (+50°) and southern (−20°) hemispheres were somewhat elevated relative to their expected values. However, in the northern hemisphere, ROSE did not observe the peak altitude abruptly increase as one would expect during a dust storm. Felici et al. (2019) suggested that the peak altitude in the northern hemisphere might have already been elevated before the ROSE observations began. Our results are consistent with this scenario since we observe the peak rise between L_s 185° and 188°, before the first ROSE observation at L_s 195°.

In summary, the peak altitude increased ∼10–15 km during the MY 34 global dust storm, and its variability increased shortly after it was elevated.

5. Discussion and Conclusions

Table 1 provides a description of the MARSIS observing conditions, the dust storm, and the response of the ionospheric peak altitude for the six case studies that were analyzed in section 4. Elevated peak altitudes were observed during each of the case studies, although in MY 29 and 32 the increases were less significant because the peak altitudes were highly variable.

The local dust storm in MY 33, the regional dust storm in MY 27, and the global dust storms in MYs 28 and 34 provided the clearest examples of elevated peak altitudes during dust storms. During the MY 27 regional dust storm, the peak altitude sharply increased by 10–15 km over ∼ 5° of L_s, and then slowly decreased back to pre-storm altitudes over ∼ 15° of L_s. This rapid rise and slow descent is consistent with previously reported observations of the thermosphere and ionosphere during dust storms (England & Lillis, 2012; Keating et al., 1998; Lillis et al., 2010; Withers & Pratt, 2013; Zurek et al., 2017). During the MY 28 global dust storm, the peak altitude also increased by 10–15 km, but the response was more gradual, occurring over ∼ 10° of L_s. The elevated peak altitudes during these storms were caused by thermospheric pressure levels rising in response to solar heating of dust, and the subsequent expansion of the lower atmosphere (Bell et al., 2007; Bougher et al., 1997; Fang et al., 2019; Hantsch & Bauer, 1990; Haberle et al., 1993; Heavens et al., 2011; Keating et al., 1998; Qin et al., 2019; Withers & Pratt, 2013; Wolkenberg et al., 2018).

During MY 33, the peak altitude increased by 10–15 km at L_s 305° and at southern latitudes between −20° and −40°. Withers et al. (2018) reported MAVEN ROSE observations showing a similar increase in the peak altitude at the same time, but at northern latitudes near +50°. They attributed the elevated peak altitude to a small, localized dust storm near the south pole. Since the MARSIS and MAVEN observations were separated by 80° in latitude, these concurrent observations suggest that this small dust storm spread quickly and affected the upper atmosphere across large distances.

Another interesting aspect of these two observations is that, after being elevated by the dust storm, the peak altitude observed by MARSIS descended more rapidly than the peak altitude observed by MAVEN ROSE. Hence, even though the dust storm was localized near the south pole, its effect on the upper atmosphere lasted longer in the northern hemisphere than in the southern hemisphere. This surprising result points to the important role of interhemispheric circulation, which allows localized dust storms to affect the upper atmosphere across the planet (Bell et al., 2007; Withers & Pratt, 2013). As shown in the model simulations (Bell et al., 2007; Medvedev et al., 2013), meridional circulation—which transfers energy from the summer hemisphere to the winter hemisphere—is enhanced by increased dust levels. The MARSIS and MAVEN ROSE observations support this result by showing that a dust storm located near the south pole during southern winter can significantly affect the upper atmosphere in both hemispheres.

Finally, from the six case studies we conclude that dust storms significantly enhance upper atmospheric variability. The clearest example is the MY 28 global dust storm, during which the peak altitude variability metric more than doubled. Substantial variability was also observed throughout the entire MY 29 and MY 32 periods, which covered the peak of the annual dust cycle near L_s 230°. Less variability was observed throughout MY 27 near L_s 315°, when dust levels were significantly lower. During the MY 34 global dust storm, the peak altitude varied by more than 20 km immediately after rising in altitude. Observations of increased upper atmospheric variability during dust storms is not unprecedented. The MGS's accelerometer observed a more than 100% increase in the orbit-to-orbit variability of thermospheric densities during the 1997 Noachis regional dust storm (Bougher et al., 1999; Keating et al., 1998).

The increased variability strongly suggests that dust storms enhance dynamical processes that couple the lower atmosphere to the upper atmosphere, such as upward propagating gravity waves or atmospheric tides (Bougher et al., 1999; England et al., 2017; Medvedev et al., 2013). Our results point to the importance of including these processes in global atmospheric models, which can successfully reproduce the neutral density and peak altitude increases observed during dust storms (Bougher et al., 1999; Bell et al., 2007; González-Galindo et al., 2010; Medvedev et al., 2013) but cannot currently reproduce the observed orbit-to-orbit variability. Refinements to these global models will improve our understanding of how dust storms affect the dynamical processes that link the lower and upper atmospheres and drive substantial thermospheric perturbations.

Acknowledgments

We thank Joe Groene and Chris Piker for helping us acquire MARSIS data using the das2py software package (https://das2.org/das2py/). We also thank an anonymous reviewer whose suggestions greatly improved the structure and content of the paper. Z. Girazian gratefully acknowledges Paul Withers, Marianna Felici, and Shane Stone for their valuable discussions. This research was supported by NASA through Contract 1560641 with the Jet Propulsion Laboratory. F. Němec was supported by MSMT Grant LTAUSA17070. The MARSIS, EUV, and dust data compiled for this study can be downloaded at https://www.researchgate.net/publication/335104578_MARSIS_EUV_DUST_DATA and are publicly available. The complete dust maps can be downloaded online (at www-mars.lmd.jussieu.fr/mars/dust_climatology/). The MCS data used in Figure 8d is publicly available and can be downloaded online (at https://atmos.nmsu.edu/data_and_services/atmospheres_data/MARS/aerosols.html).

References

Bell, J. M., Bougher, S. W., & Murphy, J. R. (2007). Vertical dust mixing and the interannual variations in the Mars thermosphere. *Journal of Geophysical Research*, *112*, E12002. https://doi.org/10.1029/2006JE002856

Bougher, S. W., Cravens, T. E., Grebowsky, J., & Luhmann, J. (2015). The aeronomy of Mars: Characterization by MAVEN of the upper atmosphere reservoir that regulates volatile escape. *Space Science Reviews*, *195*, 423–456. https://doi.org/10.1007/s11214-014-0053-7

Bougher, S. W., Engel, S., Hinson, D. P., & Forbes, J. M. (2001). Mars Global Surveyor radio science electron density profiles: Neutral atmosphere implications. *Geophysical Research Letters*, *28*, 3091–3094. https://doi.org/10.1029/2001GL012884

Bougher, S. W., Engel, S., Hinson, D. P., & Murphy, J. R. (2004). MGS radio science electron density profiles: Interannual variability and implications for the Martian neutral atmosphere. *Journal of Geophysical Research*, *109*, E03010. https://doi.org/10.1029/2003JE002154

Bougher, S., Keating, G., Zurek, R., Murphy, J., Haberle, R., Hollingsworth, J., & Clancy, R. T. (1999). Mars Global Surveyor aerobraking: Atmospheric trends and model interpretation. *Advances in Space Research*, *23*, 1887–1897. https://doi.org/10.1016/S0273-1177(99)00272-0

Bougher, S. W., Murphy, J., & Haberle, R. M. (1997). Dust storm impacts on the Mars upper atmosphere. *Advances in Space Research*, *19*, 1255–1260. https://doi.org/10.1016/S0273-1177(97)00278-0

Bougher, S. W., Pawlowski, D., Bell, J. M., Nelli, S., McDunn, T., Murphy, J. R., et al. (2015). Mars Global Ionosphere-Thermosphere Model: Solar cycle, seasonal, and diurnal variations of the Mars upper atmosphere. *Journal of Geophysical Research: Planets*, *120*, 311–342. https://doi.org/10.1002/2014JE004715

Breus, T. K., Krymskii, A. M., Crider, D. H., Ness, N. F., Hinson, D., & Barashyan, K. K. (2004). Effect of the solar radiation in the topside atmosphere/ionosphere of Mars: Mars Global Surveyor observations. *Journal of Geophysical Research*, *109*, A09310. https://doi.org/10.1029/2004JA010431

Chaffin, M. S., Deighan, J., Schneider, N. M., & Stewart, A. I. F. (2017). Elevated atmospheric escape of atomic hydrogen from Mars induced by high-altitude water. *Nature Geoscience*, *10*, 174–178. https://doi.org/10.1038/ngeo2887

Chapman, S. (1931). The absorption and dissociative or ionizing effect of monochromatic radiation in an atmosphere on a rotating Earth. *Proceedings of the Physical Society*, *43*, 26–45. https://doi.org/10.1088/0959-5309/43/1/305

Christensen, P. R., Jakosky, B. M., Kieffer, H. H., Malin, M. C., McSween, Jr., Nealson, K., et al. (2004). The Thermal Emission Imaging System (THEMIS) for the Mars 2001 Odyssey mission. *Space Science Reviews*, *110*, 85–130. https://doi.org/10.1023/B:SPAC.0000021008.16305.94

Clancy, R. T., Wolff, M. J., Whitney, B. A., Cantor, B. A., Smith, M. D., & McConnochie, T. H. (2010). Extension of atmospheric dust loading to high altitudes during the 2001 Mars dust storm: MGS TES limb observations. *Icarus*, *207*, 98–109. https://doi.org/10.1016/j.icarus.2009.10.011

Daerden, F., Neary, L., Viscardy, S., García Muñoz, A., Clancy, R. T., Smith, M. D., et al. (2019). Mars atmospheric chemistry simulations with the GEM-Mars general circulation model. *Icarus*, *326*, 197–224. https://doi.org/10.1016/j.icarus.2019.02.030

Duru, F., Gurnett, D. A., Morgan, D. D., Modolo, R., Nagy, A. F., & Najib, D. (2008). Electron densities in the upper ionosphere of Mars from the excitation of electron plasma oscillations. *Journal of Geophysical Research*, *113*, A07302. https://doi.org/10.1029/2008JA013073

England, S. L., & Lillis, R. J. (2012). On the nature of the variability of the Martian thermospheric mass density: Results from electron reflectometry with Mars Global Surveyor. *Journal of Geophysical Research*, *117*, E02008. https://doi.org/10.1029/2011JE003998

England, S. L., Liu, G., Yiğit, E., Mahaffy, P. R., Elrod, M., Benna, M., et al. (2017). MAVEN NGIMS observations of atmospheric gravity waves in the Martian thermosphere. *Journal of Geophysical Research: Space Physics*, *122*, 2310–2335. https://doi.org/10.1002/2016ja023475

Fallows, K., Withers, P., & Matta, M. (2015). An observational study of the influence of solar zenith angle on properties of the M1 layer of the Mars ionosphere. *Journal of Geophysical Research: Space Physics*, *120*, 1299–1310. https://doi.org/10.1002/2014JA020750

Fang, X., Pawlowski, D., Ma, Y., Bougher, S., Thiemann, E., Eparvier, F., Wang, W., Dong, C., Lee, C. O., Dong, Y., Benna, M., Elrod, M., Chamberlin, P., Mahaffy, P., & Jakosky, B. (2019). Mars upper atmospheric responses to the 10 September 2017 solar flare: A global, time-dependent simulation. *Geophysical Research Letters*, *46*, 9334–9343. https://doi.org/10.1029/2019GL084515

Felici, M., Withers, P., & Montabone, L. (2019). MAVEN ROSE observations of the response of the Martian ionosphere to dust storms. *Journal of Geophysical Research*.

Fox, J. L., & Weber, A. J. (2012). MGS electron density profiles: Analysis and modeling of peak altitudes. *Icarus*, *221*, 1002–1019. https://doi.org/10.1016/j.icarus.2012.10.002

Girazian, Z., & Withers, P. (2013). The dependence of peak electron density in the ionosphere of Mars on solar irradiance. *Geophysical Research Letters*, *40*, 1960–1964. https://doi.org/10.1002/grl.50344

Girazian, Z., & Withers, P. (2015). An empirical model of the extreme ultraviolet solar spectrum as a function of $F_{10.7}$. *Journal of Geophysical Research: Space Physics*, *120*, 6779–6794. https://doi.org/10.1002/2015JA021436

González-Galindo, F., Bougher, S. W., López-Valverde, M. A., Forget, F., & Murphy, J. (2010). Thermal and wind structure of the Martian thermosphere as given by two general circulation models. *Planet Space Science*, *58*, 1832–1849. https://doi.org/10.1016/j.pss.2010.08.013

Gurnett, D. A., Huff, R. L., Morgan, D. D., Persoon, A. M., Averkamp, T. F., Kirchner, D. L., et al. (2008). An overview of radar soundings of the Martian ionosphere from the Mars Express spacecraft. *Advances in Space Research*, *41*, 1335–1346. https://doi.org/10.1016/j.asr.2007.01.062

Gurnett, D. A., Kirchner, D. L., Huff, R. L., Morgan, D. D., Persoon, A. M., Averkamp, T. F., et al. (2005). Radar soundings of the ionosphere of Mars. *Science*, *310*(5756), 1929–1933. https://doi.org/10.1126/science.1121868

Guzewich, S. D., Lemmon, M., Smith, C. L., Martnez, G., de Vicente-Retortillo, Á., Newman, C. E., et al. (2019). Mars Science Laboratory observations of the 2018/Mars year 34 global dust storm. *Geophysical Research Letters*, *46*, 71–79. https://doi.org/10.1029/2018GL080839

Haberle, R. M., Pollack, J. B., Barnes, J. R., Zurek, R. W., Leovy, C. B., Murphy, J. R., et al. (1993). Mars atmospheric dynamics as simulated by the NASA AMES General Circulation Model. I—The zonal-mean circulation. *Journal of Geophysical Research*, *98*, 3093–3123. https://doi.org/10.1029/92JE02946

Hantsch, M. H., & Bauer, S. J. (1990). Solar control of the Mars ionosphere. *Planetary and Space Science*, *38*, 539–542. https://doi.org/10.1016/0032-0633(90)90146-H

Harada, Y., Gurnett, D. A., Kopf, A. J., Halekas, J. S., & Ruhunusiri, S. (2018). Ionospheric irregularities at Mars probed by MARSIS topside sounding. *Journal of Geophysical Research: Space Physics*, *123*, 1018–1030. https://doi.org/10.1002/2017JA024913

Heavens, N. G., Kleinböhl, A., Chaffin, M. S., Halekas, J. S., Kass, D. M., Hayne, P. O., et al. (2018). Hydrogen escape from Mars enhanced by deep convection in dust storms. *Nature Astronomy*, *2*, 126–132. https://doi.org/10.1038/s41550-017-0353-4

Heavens, N. G., McCleese, D. J., Richardson, M. I., Kass, D. M., & Kleinböhl, A. Schofield, J. T. (2011). Structure and dynamics of the Martian lower and middle atmosphere as observed by the Mars Climate Sounder: 2. Implications of the thermal structure and aerosol distributions for the mean meridional circulation. *Journal of Geophysical Research*, *116*, E01010. https://doi.org/10.1029/2010JE003713

Keating, G. M., Bougher, S. W., Zurek, R. W., Tolson, R. H., Cancro, G. J., Noll, S. N., et al. (1998). The structure of the upper atmosphere of Mars: In situ accelerometer measurements from Mars Global Surveyor. *Science*, *279*, 1672. https://doi.org/10.1126/science.279.5357.1672

Krasnopolsky, V. A. (2019). Photochemistry of water in the Martian thermosphere and its effect on hydrogen escape. *Icarus*, *321*, 62–70. https://doi.org/10.1016/j.icarus.2018.10.033

Lillis, R. J. Bougher, S. W. Gonzlez-Galindo, F. Forget, F. Smith, M. D. & Chamberlin, P. C. (2010). Four Martian years of nightside upper thermospheric mass densities derived from electron reflectometry: Method extension and comparison with GCM simulations. *Journal of Geophysical Research*, *115*, E07014. https://doi.org/10.1029/2009JE003529

Liu, G., England, S. L., Lillis, R. J., Withers, P., Mahaffy, P. R., Rowland, D. E., et al. (2018). Thermospheric expansion associated with dust increase in the lower atmosphere on Mars observed by MAVEN/NGIMS. *Geophysical Research Letters*, *45*, 2901–2910. https://doi.org/10.1002/2018GL077525

Mahaffy, P. R., Benna, M., Elrod, M., Yelle, R. V., Bougher, S. W., Stone, S. W., & Jakosky, B. M. (2015). Structure and composition of the neutral upper atmosphere of Mars from the MAVEN NGIMS investigation. *Geophysical Research Letters*, *42*, 8951–8957. https://doi.org/10.1002/2015GL065329

McCleese, D. J., Schofield, J. T., Taylor, F. W., Calcutt, S. B., Foote, M. C., Kass, D. M., et al. (2007). Mars Climate Sounder: An investigation of thermal and water vapor structure, dust and condensate distributions in the atmosphere, and energy balance of the polar regions. *Journal of Geophysical Research*, *112*, E05S06. https://doi.org/10.1029/2006JE002790

McElroy, M. B., Kong, T. Y., & Yung, Y. L. (1977). Photochemistry and evolution of Mars' atmosphere: A Viking perspective. *Journal of Geophysical Research*, *82*, 4379–4388. https://doi.org/10.1029/JS082i028p04379

Medvedev, A. S., Yiğit, E., Kuroda, T., & Hartogh, P. (2013). General circulation modeling of the Martian upper atmosphere during global dust storms. *Journal of Geophysical Research: Planets*, *118*, 2234–2246. https://doi.org/10.1002/2013JE004429

Mendillo, M., Narvaez, C., Vogt, M. F., Mayyasi, M., Forbes, J., Galand, M., et al. (2017). Sources of ionospheric variability at Mars. *Journal of Geophysical Research: Space Physics*, *122*, 9670–9684. https://doi.org/10.1002/2017JA024366

Montabone, L., Forget, F., Millour, E., Wilson, R. J., Lewis, S. R., Cantor, B., et al. (2015). Eight-year climatology of dust optical depth on Mars. *Icarus*, *251*, 65–95. https://doi.org/10.1016/j.icarus.2014.12.034

Montabone, L., Spiga, L., Kass, D., Kleinböhl, A., Forget, F., & Ehouarn, M. (2019). Martian year 34 column dust climatology from Mars Climate Sounder observations: Reconstructed maps and model simulations. *Journal of Geophysical Research*. https://doi.org/arXiv:1907.08187

Morgan, D. D., Gurnett, D. A., Kirchner, D. L., Fox, J. L., Nielsen, E., & Plaut, J. J. (2008). Variation of the Martian ionospheric electron density from Mars Express radar soundings. *Journal of Geophysical Research*, *113*, A09303. https://doi.org/10.1029/2008JA013313

Němec, F., Morgan, D. D., & Gurnett, D. A. (2016). On improving the accuracy of electron density profiles obtained at high altitudes by the ionospheric sounder on the Mars Express spacecraft. *Journal of Geophysical Research: Space Physics*, *121*, 10,117–10,129. https://doi.org/10.1002/2016JA023054

Picardi, G., Biccari, D., Seu, R., Plaut, J., Johnson, W. T. K., Jordan, R. L., et al. (2004). MARSIS: Mars advanced radar for subsurface and ionosphere sounding. In A. Wilson (Ed.), *Mars Express: A European mission to the red planet, SP-1240* (pp. 51–70). Noordwijk, Netherlands: European Space Agency Publication Division.

Qin, J. F., Zou, H., Ye, Y. G., Yin, Z. F., Wang, J. S., & Nielsen, E. (2019). Effects of local dust storms on the upper atmosphere of Mars: Observations and simulations. *Journal of Geophysical Research: Planets*, *124*, 602–616. https://doi.org/10.1029/2018JE005864

Sánchez-Lavega, A., del Ro-Gaztelurrutia, T., Hernndez-Bernal, J., & Delcroix, M. (2019). The onset and growth of the 2018 Martian global dust storm. *Journal of Geophysical Research: Planets*, *46*, 6101–6108. https://doi.org/10.1029/2019GL083207

Schunk, R. W., & Nagy, A. F. (2009). *Ionospheres* (Second). New York: Cambridge University Press.

Siddle, A. G., Mueller-Wodarg, I. C. F., Stone, S. W., & Yelle, R. V. (2019). Global characteristics of gravity waves in the upper atmosphere of Mars as measured by MAVEN/NGIMS. *Icarus*, *333*, 12–21. https://doi.org/10.1016/j.icarus.2019.05.021

Terada, N., Leblanc, F., Nakagawa, H., Medvedev, A. S., Yiğit, E., Kuroda, T., et al. (2017). Global distribution and parameter dependences of gravity wave activity in the Martian upper thermosphere derived from MAVEN/NGIMS observations. *Journal of Geophysical Research: Space Physics*, *122*, 2374–2397. https://doi.org/10.1002/2016JA023476

Thiemann, E. M. B., Chamberlin, P. C., Eparvier, F. G., Templeman, B., Woods, T. N., Bougher, S. W., & Jakosky, B. M. (2017). The MAVEN EUVM model of solar spectral irradiance variability at Mars: Algorithms and results. *Journal of Geophysical Research: Space Physics*, *122*, 2748–2767. https://doi.org/10.1002/2016JA023512

Thiemann, E. M. B., Eparvier, F. G., Bougher, S. W., Dominique, M., Andersson, L., Girazian, Z., et al. (2018). Mars thermospheric variability revealed by MAVEN EUVM Solar Occultations: Structure at aphelion and perihelion and response to EUV forcing. *Journal of Geophysical Research: Planets*, *123*, 2248–2269. https://doi.org/10.1029/2018JE005550

Vandaele, A. C., Korablev, O., Daerden, F., Aoki, S., Thomas, I. R., Altieri, F., et al. (2019). Martian dust storm impact on atmospheric H_2O and D/H observed by ExoMars Trace Gas Orbiter. *Nature*, *568*(7753), 521–525. https://doi.org/10.1038/s41586-019-1097-3

Vogt, M. F., Withers, P., Fallows, K., Andersson, L., Girazian, Z., Mahaffy, P. R., et al. (2017). MAVEN observations of dayside peak electron densities in the ionosphere of Mars. *Journal of Geophysical Research: Space Physics*, *122*, 891–906. https://doi.org/10.1002/2016JA023473

Wang, J.-S., & Nielsen, E. (2003). Behavior of the Martian dayside electron density peak during global dust storms. *Planetary and Space Science*, *51*, 329–338. https://doi.org/10.1016/S0032-0633(03)00015-1

Withers, P. (2006). Mars Global Surveyor and Mars Odyssey Accelerometer observations of the Martian upper atmosphere during aerobraking. *Geophysical Research Letters*, *33*, L02201. https://doi.org/10.1029/2005GL024447

Withers, P. (2009). A review of observed variability in the dayside ionosphere of Mars. *Advances in Space Research*, *44*, 277–307. https://doi.org/10.1016/j.asr.2009.04.027

Withers, P., Felici, M., Mendillo, M., Moore, L., Narvaez, C., Vogt, M. F., & Jakosky, B. M. (2018). First ionospheric results from the MAVEN Radio Occultation Science Experiment (ROSE). *Journal of Geophysical Research: Space Physics*, *123*, 4171–4180. https://doi.org/10.1029/2018JA025182

Withers, P., & Pratt, R. (2013). An observational study of the response of the upper atmosphere of Mars to lower atmospheric dust storms. *Icarus*, *225*, 378–389. https://doi.org/10.1016/j.icarus.2013.02.032

Wolkenberg, P., Giuranna, M., Grassi, D., Aronica, A., Aoki, S., Scaccabarozzi, D., & Saggin, B. (2018). Characterization of dust activity on Mars from MY27 to MY32 by PFS-MEX observations. *Icarus*, *310*, 32–47. https://doi.org/10.1016/j.icarus.2017.10.045

Zou, H., Lillis, R. J., Wang, J. S., & Nielsen, E. (2011). Determination of seasonal variations in the Martian neutral atmosphere from observations of ionospheric peak height. *Journal of Geophysical Research*, *116*, E09004. https://doi.org/10.1029/2011JE003833

Zou, H., Ye, Y. G., Wang, J. S., Nielsen, E., Cui, J., & Wang, X. D. (2016). A method to estimate the neutral atmospheric density near the ionospheric main peak of Mars. *Journal of Geophysical Research: Space Physics*, *121*, 3464–3475. https://doi.org/10.1002/2015JA022304

Zurek, R. W., Tolson, R. A., Bougher, S. W., Lugo, R. A., Baird, D. T., Bell, J. M., & Jakosky, B. M. (2017). Mars thermosphere as seen in MAVEN accelerometer data. *Journal of Geophysical Research: Space Physics*, *122*(3), 3798–3814. https://doi.org/10.1002/2016JA023641